Investigation of capillary nanosecond discharges in air at moderate pressure: comparison of experiments and 2D numerical modelling

Andrei V Klochko[1,4]**, Svetlana M Starikovskaia**[1]**, Zhongmin Xiong**[2,3]
and Mark J Kushner[2]

[1] Laboratory of Plasma Physics (CNRS, Ecole Polytechnique, Sorbonne Universities, UPMC Univ. Paris 06, University Paris-Sud) Palaiseau, 91128, France

[2] University of Michigan, Electrical Engineering and Computer Science Department, Ann Arbor, MI 48109, USA

E-mail: andrei.klochko@polytechnique.edu, svetlana.starikovskaya@lpp.polytechnique.fr, zxiong@umich.edu and mjkush@umich.edu

Abstract

Nanosecond electrical discharges in the form of ionization waves are of interest for rapidly ionizing and exciting complex gas mixtures to initiate chemical reactions. Operating with a small discharge tube diameter can significantly increase the specific energy deposition and so enable optimization of the initiation process. Analysis of the uniformity of energy release in small diameter capillary tubes will aid in this optimization. In this paper, results for the experimentally derived characteristics of nanosecond capillary discharges in air at moderate pressure are presented and compared with results from a two-dimensional model. The quartz capillary tube, having inner and outer diameters of 1.5 and 3.4 mm, is about 80 mm long and filled with synthetic dry air at 27 mbar. The capillary tube with two electrodes at the ends is inserted into a break of the central wire of a long coaxial cable. A metal screen around the tube is connected to the cable ground shield. The discharge is driven by a 19 kV 35 ns voltage pulse applied to the powered electrode. The experimental measurements are conducted primarily by using a calibrated capacitive probe and back current shunts. The numerical modelling focuses on the fast ionization wave (FIW) and the plasma properties in the immediate afterglow after the conductive plasma channel has been established between the two electrodes. The FIW produces a highly focused region of electric field on the tube axis that sustains the ionization wave that eventually bridges the electrode gap. Results from the model predict FIW propagation speed and current rise time that agree with the experiment.

Keywords: capillary discharge, air plasma, nanosecond voltage pulse, fast ionization wave, numerical simulation

(Some figures may appear in colour only in the online journal)

1. Introduction

Plasma discharges produced by nanosecond voltage pulses are attractive for applications from plasma assisted combustion to aerodynamic flow control at high Mach number [1, 2]. This utility results from such discharges having a low power requirement (pulsed nature) with a high energy efficiency for producing radicals and electronically excited species, which in turn can contribute to fast gas heating [3, 4].

To characterize the ensuing plasma and chemical processes in repetitively pulsed nanosecond discharges (for

[3] Present address: ESI US R&D, 32605 W 12 Mile Road, Suite 350, Farmington Hills, MI 48334, USA, E-mail: zax@esi-group.com.
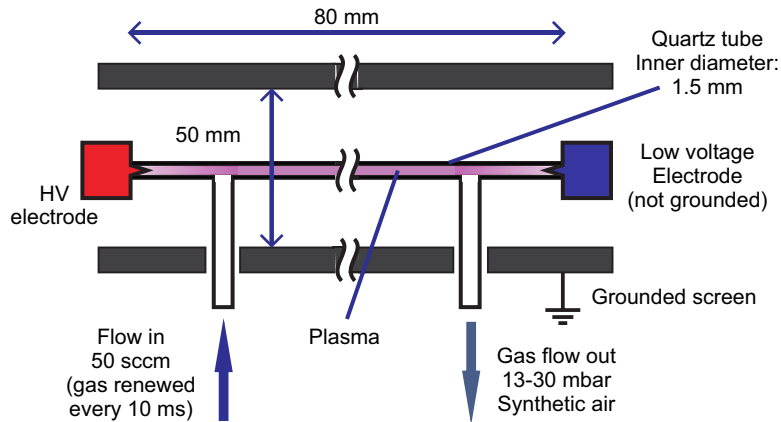[4] Author to whom any correspondence should be addressed.

Figure 1. Schematic of the discharge tube assembly.

example, the radicals [5] and excited species [6] production, energy deposition and gas heating) [7, 8], it is important to understand the initial breakdown process [9] which, at moderate pressures, is usually in the form of a fast ionization wave (FIW) [10]. FIWs are produced and propagate when the discharge is over-voltaged by hundreds of percent. Over-voltage refers to conditions where the voltage applied to the electrodes is much greater than the quasi-dc breakdown voltage at given gas density. It is during the FIW breakdown process that the initial density and energy distribution of the charged and excited species in the plasma are generated. These high energy populations then relax in the afterglow by following reaction paths that depend on the specific plasma chemistry for the intended application. Understanding the FIW discharge is also an important step in controlling and optimizing the plasma. As a result, there is ongoing research on the dynamics of FIW discharges. Much of our current knowledge about FIWs comes from experiments conducted in straight tubes [10, 11] and from analytic and numerical models [12, 13].

The detailed dynamics of FIW discharges are still not completely understood. For example, there is little verification of the transverse electronic structure of the FIWs inside a tube. This situation is mainly due to the difficulty of experimentally measuring the fast propagation speed of the FIW, on the order of a few $cm\,ns^{-1}$ ($10^9\,cm\,s^{-1}$), and the difficulty in measuring the electron density and electric field *inside* the tube without significantly disturbing the FIW itself. To investigate FIWs at high specific energy deposition, capillary discharges are used, with a tube diameter of the order of 1 mm [14]. This makes the direct measurements of the FIW and plasma properties even more challenging. Consequently, much can be gained by using a collaborative approach between experiments and numerical modelling.

In this paper, we present the results from a joint experimental and numerical investigation of a nanosecond discharge inside a capillary tube filled with synthetic air at moderate pressure and initially at room temperature. The main purpose of the study is to better understand the dynamics of capillary FIWs as well as the reliability of hydrodynamic plasma models for simulating such discharges. In section 2, a brief description of the experimental setup and diagnostics is presented, followed by a description of the numerical model

and simulation conditions. In section 3, the experimental results are presented with comparison to results from the model, focusing on the electronic structure of the FIWs and the plasma properties in such discharges. The concluding remarks are given in section 4.

2. Descriptions of the experiments and numerical model

2.1. The capillary nanosecond discharge

The experimental setup and conditions are discussed in detail in [14] and so only a brief description is given here. Schematics and images of the experiment setup, along with one diagnostic (capacitive probe) for the capillary nanosecond discharge are shown in figures 1 and 2(*a*). The equivalent circuit for the capacitive probe used to measure the local electric potential is shown in figure 2(*b*). The discharge is initiated inside an 80 mm long capillary quartz tube with inner and outer diameters of 1.5 and 3.4 mm. Synthetic dry air ($N_2 : O_2 = 4 : 1$, purity 99.9999%) flows inside the capillary at a pressure of 27 mbar with a fixed flow rate of 50 sccm, ensuring gas renewal between pulses. Two grounded aluminium plates enclose the capillary from above and below with a 48 mm separation. Adhesive aluminium sheets complete this construction to form a closed, grounded screen having a rectangular cross section (48×60 mm). The discharge tube is terminated by two metal pin-shaped high (HV) and low (LV) voltage electrodes that are connected to two cables. A 25 m long coaxial RG213 cable connects the HV electrode to a FID FPG 10-MKS20 HV generator that supplies the voltage pulses (29 ns FWHM, 9.8 kV amplitude, and 4 ns rise time). A 10 Hz repetition frequency was used for all of the experiments. The other cable, connected to the LV electrode, is left unterminated.

Two electrical diagnostics were used for the experimental measurements – back current shunts (BCS) and a capacitive probe. The BCS [15] consists of an array of 12 identical 2.2 Ω low-inductance resistors soldered into a break in the ground shield of a long coaxial cable. The voltage on the resistors is measured and related to the current flowing through the cable, and to the voltage between the central wire and the cable shield. Calibration of the current shunt is made based
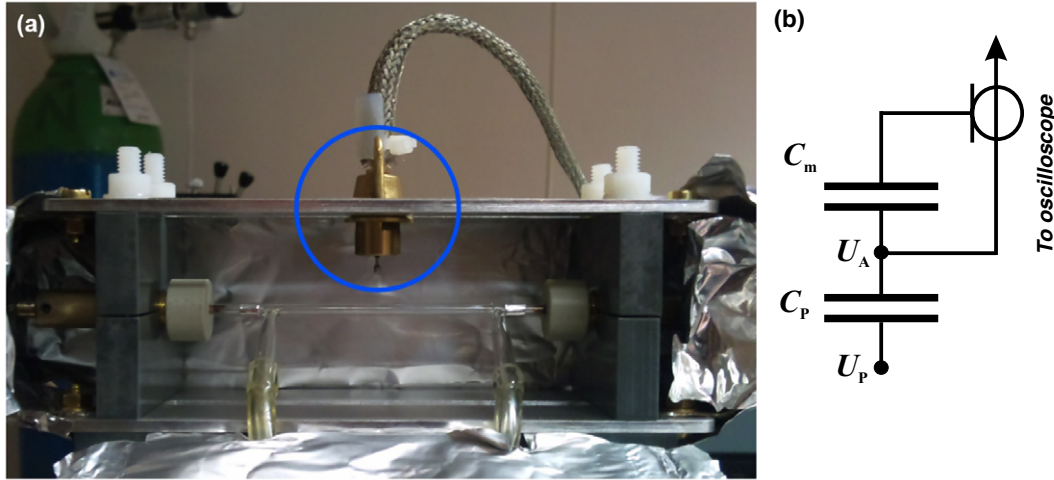
Figure 2. Experimental setup. (*a*) Image of the discharge apparatus, with one side of the aluminium screen open. The capacitive probe is circled in blue. The conical electrodes are small tips protruding from the grey dielectric caps used for vacuum sealing. (*b*) Equivalent circuit of the capacitive probe. U_p is the potential at the inner surface of the tube and U_A is the potential of the probe tip, C_p is the capacitance between the probe tip and the tube inner surface, and C_m is the capacitance of a coaxial capacitor located inside the probe.

on measurements of a known high voltage (for amplitude calibration) and a known nanosecond pulse shape (for time calibration).

The capacitive probe, inserted in a slit of the upper part of the screen, provides local voltage measurements at different axial locations (with mm resolution) above the discharge. The metal tip of the probe, which protrudes from the grounded screen to 12.7 mm from the tube axis, is at floating potential and connected through a 400 pF coaxial capacitor to a 50 Ω oscilloscope input. Using the equivalent circuit of the capacitive probe shown in figure 2(*b*), the electric potential U_A measured at the detector is related to the potential at the inner surface U_p of the discharge tube by,

$$U_\mathrm{A} = \frac{U_\mathrm{p} i\omega C_\mathrm{p}}{\frac{1}{R} + i\omega C_\mathrm{m} + i\omega C_\mathrm{p}}, \tag{1}$$

$$U_\mathrm{p} = U_\mathrm{A}\left(\left(1 + \frac{C_\mathrm{m}}{C_\mathrm{p}}\right) + \frac{1}{i\omega R C_\mathrm{p}}\right), \tag{2}$$

$$U_\mathrm{p}(t) = \alpha\left(U_\mathrm{A}(t) + \frac{1}{\tau}\int_{t'=0}^{t} U_\mathrm{A}(t')\,\mathrm{d}t'\right),$$

$$\alpha = 1 + \frac{C_\mathrm{m}}{C_\mathrm{p}}, \quad \tau = R\left(C_\mathrm{m} + C_\mathrm{p}\right) \tag{3}$$

where C_m is the capacitance of the coaxial capacitor in the capacitive probe, C_p is the capacitance between the capacitive probe tip and plasma, and R is the cable impedance, which is matched with the oscilloscope input resistor. To calibrate the probe, the air plasma is replaced by a 1 mm diameter copper wire connecting the HV and LV electrodes. The rest of the system remains unchanged. A HV pulse is transmitted without significant loss from the HV to the LV electrode so that the potential at the surface of the wire is close to that provided by the generator, and the potential at the inner surface of the capillary tube (1.5 mm diameter) is therefore known. The two parameters α and τ are then adjusted so that the signal produced by the capacitive probe closely agrees with the values extracted from the shunt probe measurements. By

this process, an absolute calibration of the capacitive probe is made. Finally, during experiments with the plasma, detector signals at different axial locations are assembled to provide voltage profiles, and then differentiated to produce the value of the local electric field.

2.2. Two-dimensional plasma hydrodynamics model

The two-dimensional (2D) simulations of nanosecond discharges in the capillary tube were performed using *nonPDPSIM,* a plasma hydrodynamics model with radiation transport [16, 17]. Based on 2D unstructured finite volume discretization, *nonPDPSIM* solves the transport equations for all charged species and Poisson's equation for electric potential using a fully implicit Newton's method. Updates of the charged particle densities and electric potential are followed by an implicit update of the electron temperature, T_e, neutral particle densities, kinetic transport for secondary electrons and neutral flow field properties using a modified version of the Navier–Stokes equations. In the present study, the plasma species included in the model are the ground states of N_2, O_2, N, O and O_3, the N_2 vibrational states ($v = 1$–8), five excited states (N_2^*, O_2^*, N_2^{**}, N^*, O^*), and nine charged species (e, N_2^+, O_2^+, N^+, O^+, N_4^+, O_4^+, O_2^-, O^-). The total number of reactions in the mechanism is 180. To facilitate the propagation of the positive ionization wave, photoionization of O_2 by the VUV flux from the radiating N_2^{**} (Birge–Hopfield band, $b'^1\Sigma_u^+$, $b^1\Pi_u \rightarrow X^1\Sigma_g^+$) was included with a cross-section varying between 1 to $5 \times 10^{-16}\,\mathrm{cm}^2$. Secondary electron emission from plasma bounding surfaces due to ion bombardment was also included with a secondary emission coefficient $\gamma = 0.1$. The secondary electron emission produced by photon bombardment was neglected for simplicity.

The discharge configuration used in the 2D model is based on the experimental setup but assumed to be axisymmetric. The geometry includes the HV and LV electrodes, the grounded metal screen shield having a radius of 2.5 cm and the discharge
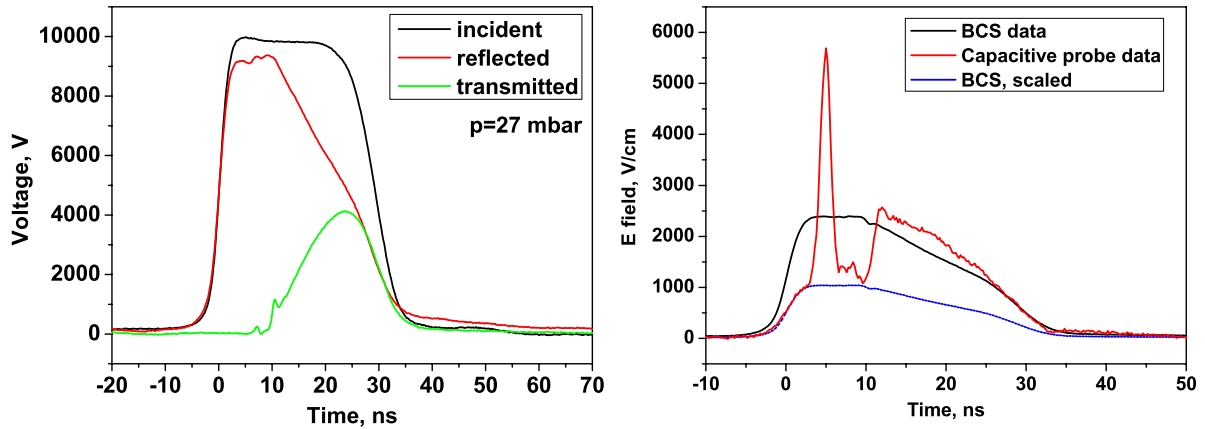
Figure 3. Experimental discharge characteristics. (*a*) Incident, reflected and transmitted voltage pulses, measured by the BCS. (*b*) Electric field, locally measured by the capacitive probe, and estimated from BCS data. The blue curve corresponds to the electric field from BCS data, scaled to fit the initial phase of the experiment, when voltage is applied but the FIW has not started yet, between −2 and 3 ns.

capillary quartz tube ($\varepsilon_r = 4$). The inner and outer diameters of the capillary are 0.15 and 0.34 cm, and the distance between HV and LV electrode tips is 8 cm. The capillary is filled with synthetic air ($N_2 : O_2 = 4 : 1$) at 27 mbar and 300 K and the forced gas flow is neglected. Note that because of the axisymmetric nature of the calculation, the metal shield in the model is cylindrical instead of the screen with 4.8×6 cm rectangular cross section used in the experiments. A 20 kV voltage pulse of 35 ns length (about 6 ns rise time and 8 ns fall time) was applied to the HV electrode to initiate and sustain the discharges. The initial electron density was assumed to be $[e] = 10^9 \text{ cm}^{-3}$ uniformly distributed in the capillary to account for the residual electron density from prior pulses that occurs in the experiment. The total number of grid points in the numerical mesh was about 20 000, of which about 15 000 are distributed in the plasma zone with the mesh size varying between 50 and 100 μm.

There is some sensitivity to the choice of initial conditions and simulation parameters. If the preionization density is significantly larger than $[e] = 10^9 \text{ cm}^{-3}$, the plasma column is too conductive at the application of the initial voltage, and FIW behaviour is compromised. If the preionization density is significantly lower than $[e] = 10^9 \text{ cm}^{-3}$, then there is longer delay in the onset of current than is experimentally observed. There is also a sensitivity to the choice of photo-ionization cross section. The peak current during the discharge pulse is sensitive to the choice of photo-ionization cross sections, and increases with increasing photoionization cross section. The value used in the model corresponds to a mean-free-path for absorption of 4 μm. There is little sensitivity to the choice of secondary electron emission coefficient (factors of 2 larger or smaller).

3. Dynamics of the capillary FIW discharge

The incident, reflected and transmitted voltages obtained from the BCS are shown in figure 3(*a*). The incident and reflected waveforms were measured using a BCS on the HV side, whereas the transmitted waveform was measured using a BCS on the LV side. The incident and reflected waveforms in

the figure have been adjusted to correlate in time, taking into account the length of the cables and the speed of the discharge propagation. The voltage on the HV electrode corresponds to the summation of the incident and reflected voltages, and this value is used as the voltage input to the numerical model. The reduced electric field E/N (1 Td = 10^{-17} V cm^2), locally measured by the capacitive probe and estimated on the basis of the difference between the HV and LV electrode potentials obtained from the BCS measurements, is shown in figure 3(*b*). In producing the last curve, we maintained that the voltage and current in the cable are related by $U = IZ$, where $Z = 50 \, \Omega$ is the wave resistance of the cable. An additional curve in the figure represents a scaled version of the estimated field. This scaled version represents the initial phase of the discharge when the FIW has not started yet and the electric field is given by its vacuum values. Once the FIW starts, the high and narrow peak in E/N of about 750 Td at $t = 5$ ns corresponds to the passing of the FIW near the capacitive detector. Finally, the time interval between 13 and 33 ns corresponds to the energy deposition phase having a high current with a still high (around 200 Td), spatially uniform electric field. The local field then roughly follows the global, unscaled field, because of the conductive nature of the plasma channel connecting the two electrodes.

The electron impact ionization source S_e and electric potential φ computed with the model are shown in figure 4 for 27 mbar pressure at $t = 3.0$, 5.6 and 8.0 ns. The computational domain shown here includes the tube wall (top) and part of the HV (left) and LV (right) electrodes. Note that the radial scale has been expanded by a factor of 18 so that detail in the capillary tube can be observed which would otherwise be obscured by the large aspect ratio of the capillary. During its propagation, the structure of the ionization front does not significantly change and the peak value of S_e remains on the axis. However, the magnitude of the peak S_e increases from $3.4 \times 10^{24} \text{ cm}^{-3} \text{ s}^{-1}$ near the HV electrode to $1.4 \times 10^{25} \text{ cm}^{-3} \text{ s}^{-1}$ near the LV electrode. This increase is partly because the voltage on the HV electrode rises between $t = 0–6$ ns, which produces a small region of additional ionization near the HV electrode at $t = 5.6$ ns.
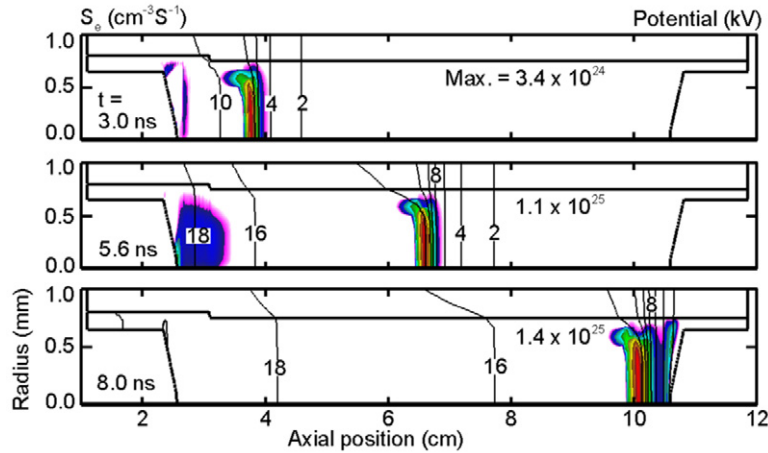
Figure 4. The electron impact ionization rate S_e and the electric potential φ at $t = 3.0$, 5.6 and 8.0 ns during the FIW discharge in the capillary. The high and low voltage electrodes are located at the left and right ends of the tube and the top is the dielectric tube wall. Contours are on a log scale over 4 decades.
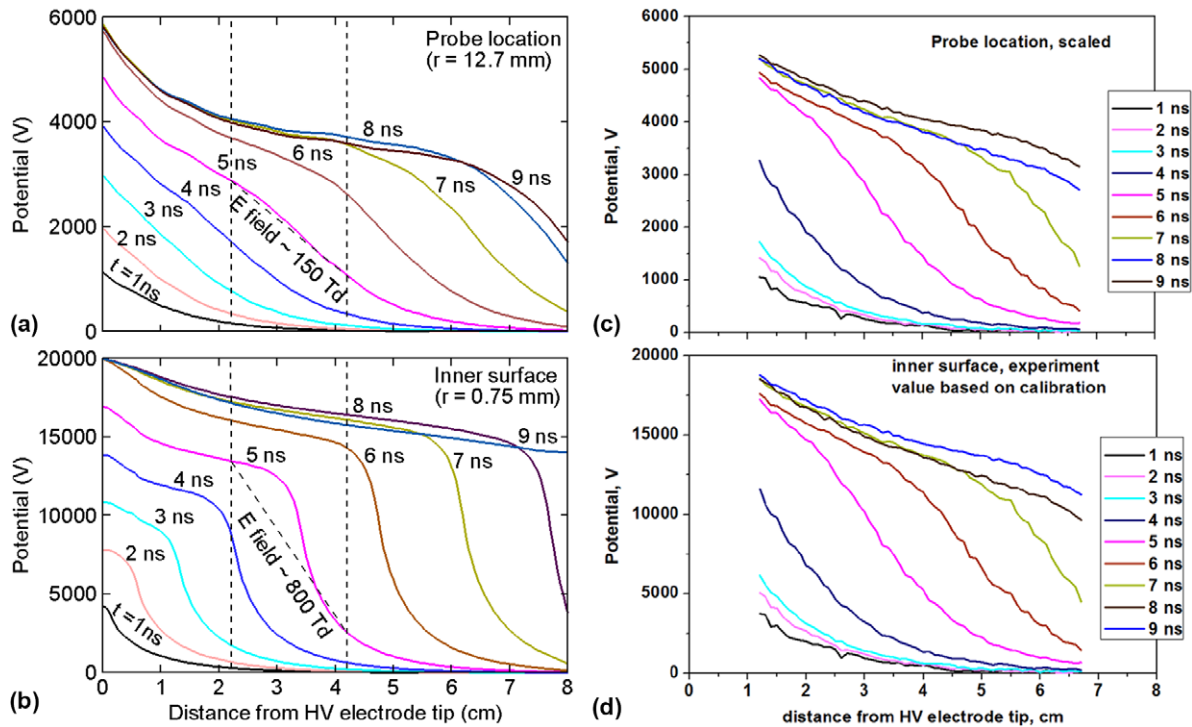

Figure 5. Axial potential profiles obtained from the model at (*a*) the tip of the capacitive probe in the experiments, $r = 12.7$ mm, and (*b*) the inner surface of the capillary, $r = 0.75$ mm. The two vertical dash lines mark the region between $z = 22$ and 42 mm from the HV tip where the electric field is measured in the experiments. Experimental curves are shown in (*c*) scaled to match the numerical values and (*d*) based on experimental calibration as described in section 2.

The increase is also partly a result of the decreasing distance between the FIW front and the LV electrode, which produces a continuously increasing electric field in front of the FIW as the LV electrode is approached. This latter effect can be seen from the tight clustering of the potential contour lines in front of the FIW at $t = 8.0$ ns.

Experimental measurements and model predictions of the electric potential $\varphi(z)$ as a function of the axial distance z (measured from the tip of the HV electrode) are shown in figure 5 at times $t = 1$–9 ns. Values from the model are shown at two radial locations—at the tip of the capacitive

probe, $r = 1.27$ cm (figure 5(*a*)), and the inner surface of the capillary, $r = 0.075$ cm (figure 5(*b*)). Experimental curves are shown scaled to match the $r = 1.27$ cm numerical values, in figure 5(*c*), and in absolute values (based on the calibration with the copper wire) in figure 5(*d*). The FIW front speeds derived from the modelling and from the experiments, about 1.4 mm ns^{-1}, show good agreement.

During the propagation of the FIW, the shapes of the $\varphi(z)$ profiles at the probe location predicted by the model are quite similar to the scaled experimental profiles. The profiles are rather smooth and lack sharp gradients. If one estimates the

J. Phys. D: Appl. Phys. **47** (2014) 365202

A V Klochko *et al*

peak reduced electrical field in figure 5(*a*) (1.27 cm off axis) using $\varphi(z)$ at $t = 5$ ns and between $z = 2.2$ and 4.2 cm from the electrode (the two vertical dashed lines) as in the experiments, E/N is about 150 Td. Taking into account the scaling factor for potential ($\sim$4.8) between figures 5(*c*) and (*d*), this corresponds to a peak E/N of approximately 720 Td, which is close to the measured peak E/N value in figure 3(*b*). This agreement suggests that the FIW dynamics captured by the present 2D modelling are consistent with those in the experiments.

While in the experiments, $\varphi(z)$ profiles along the inner capillary surface ($r = 0.75$ mm) need to be inferred from the capacitive probe measurements, they can be obtained directly in the simulations as shown in figure 5(*b*). Compared to $\varphi(z)$ at the position of the probe, the primary difference between $\varphi(z)$ at the two radii is that the $\varphi(z)$ profiles on the inner surface show sharper gradient in potential moving from left to right. These sharp gradients correspond to the instantaneous axial locations of the FIW. If one again estimates the peak E/N in the same region between $z = 2.2$ and 4.2 cm directly using the $\varphi(z)$ in figure 5(*b*) (without the scaling factor), the spatially averaged E/N is about 800 Td, which is only slightly higher than the experimental value. We note the maximum E/N in this region at the leading edge of the FIW is about 2000 Td. However, given the fast speed of the FIW and the finite spatial and temporal resolution of the capacitive probe, the averaged E/N value is probably a more useful quantity to compare with the experiments.

The lack of sharp gradients for the potential curves at the location of the probe is not unexpected. From a physical point of view, inside the capillary tube the FIW front separates an ionized, conductive region behind the FIW from the neutral, non-conductive region in front of the FIW. The potential at the FIW at the leading edge of the conductive channel is essentially the HV potential (minus the voltage drop due to the plasma resistivity). A large voltage drop occurs across the FIW. At the location of the probe, there is no such separation between ionized and non-ionized regions since the ambient air remains neutral and acts simply as a dielectric. From a computational viewpoint, there is a large contribution of space charge inside the capillary to Poisson's equation which is capable of producing sharp potential gradients, while at the probe location, the lack of space charge reduces the Poisson's equation to a homogeneous Laplace equation, which tends to produce smooth solutions.

To better characterize the electronic structure of the FIW, the computed axial and radial electric fields E_z and E_r, and the electron density n_e near the FIW head are shown in figure 6 at $t = 5$ ns.

While E_z at the inner surface of the tube is about 20 kV cm^{-1}, its peak value on the axis is higher, about 45 kV cm^{-1}. Slightly behind the FIW front, there is a narrow and elongated region near the wall where the radial electric field E_r reaches its peak, around 100 kV cm^{-1}, significantly higher than that of E_z, as a consequence of wall charging and sheath formation. The high E_r in this region may be understood from the spatial profile of n_e. The plasma channel that occupies the central region of the capillary has a high electron density $n_e = 5.4 \times 10^{14}$ cm^{-3}, and high conductivity. As a result, the
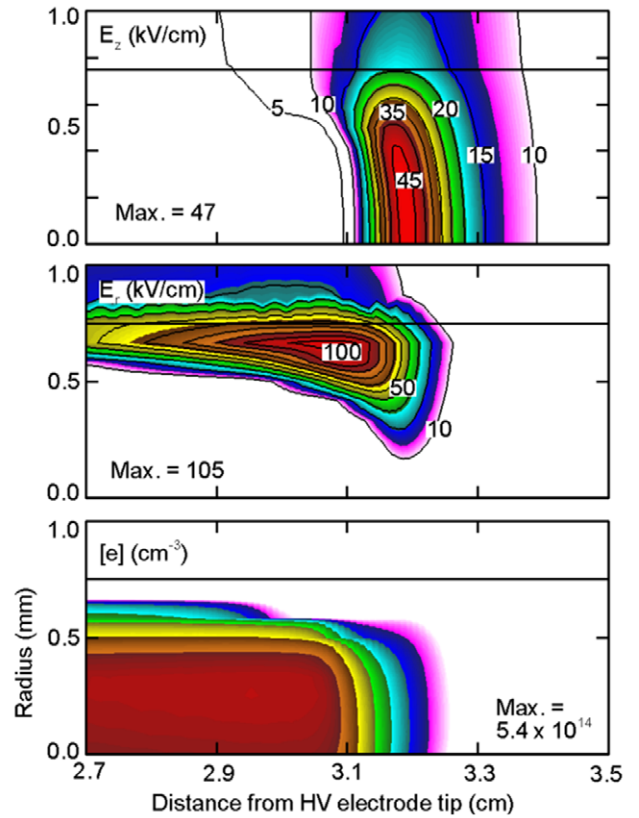

Figure 6. The instantaneous axial (*a*) and radial (*b*) electric fields E_z and E_r and the electron density n_e (*c*) at the FIW front at $t = 5$ ns, with an expanded radial scale. Contours are on a log scale over 4 decades. The quartz tube is at $r > 0.75$ mm.

electric potential within the plasma column is close to the HV voltage. So there exists a large potential difference in the radial direction between the outer edge of the plasma channel and the wall of the tube, culminating in the sheath, which results in a large E_r.

To assess the spatial uniformity of the plasma produced by the FIW, emission from the discharge was captured with a nanosecond intensified charge-coupled device (ICCD) camera (ANDOR iStar DH-734-18U-03) observing the emission of the second positive system of molecular nitrogen, $N_2(C^3\Pi_u, v' = 0) \rightarrow N_2(B^3\Pi_g, v = 0)$. The population of the upper level is largely due to direct electron impact. The life time of $N_2(C^3\Pi_u, v' = 0)$ is determined by quenching and is about 15 ns. As the quenching time is much less than the diffusion time to the walls, the emission of the second positive system can be used as a reference of the discharge spatial uniformity. A Typical ICCD image taken with a 10 ns gate is in figure 7(*a*). The radial profile of the emission was averaged within the area bordered in red to decrease the signal-to-noise ratio.

To compare experimental and numerical results, the calculated profiles of $N_2(C^3\Pi_u, v' = 0)$ emission were integrated along the chords, in accordance with the Abel transform procedure. A comparison of calculated and measured profiles is in figure 7(*b*). In spite of some difference in the wings, both calculations and measurements confirm non-streamer, volumetric structure of plasma in the capillary tube.
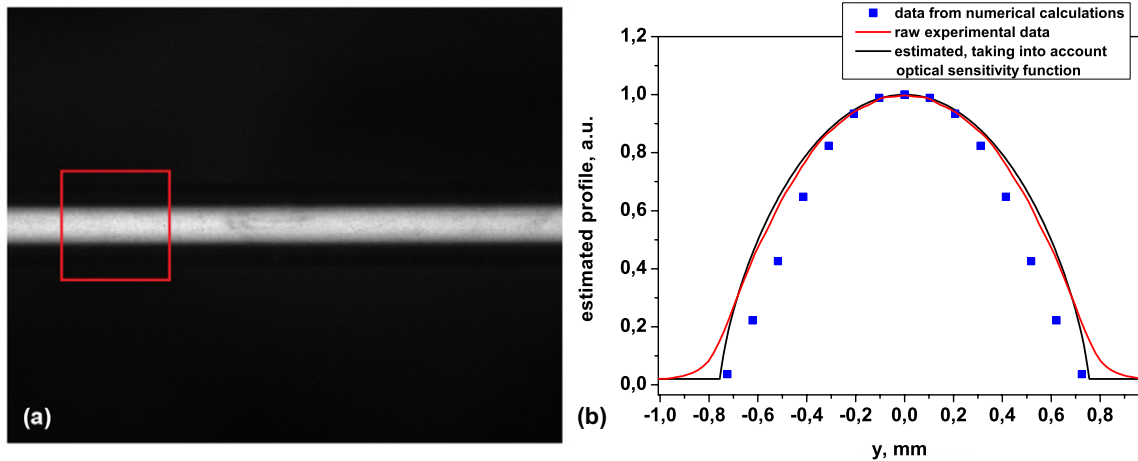
Figure 7. Distribution of emission of the second positive system of molecular nitrogen in the capillary tube: (*a*) ICCD image of the discharge afterglow, 50 ns after the beginning of the HV pulse. The exposure time is 10 ns. The radial profile of the intensity was averaged in the area bordered in red. (*b*) Comparison of calculated and measured normalized radial emission profiles. The red and black lines are extracted from experimental data, whereas the blue values are obtained from the 2D model results.

The computed time dependence of the transmitted current, and the axial and radial electric fields at $z = 3.2$ cm on the tube axis and the inner surface of the wall are shown in figure 8. The computed current has a similar shape to that found in the experiments, as shown in figure 3(*b*). The peak value of around 90 A also compares favourably with the measurements. As in figure 3(*b*), there are two small peaks in the computed current around $t = 8.5$ ns and 10.5 ns. The first peak represents the arrival of the FIW front at the LV electrode whereas the second peak is the return strike, in which the LV electrode launches a secondary ionization wave that travels backward towards the HV electrode with a high speed inside the already formed plasma channel. The closing of the gap by the forward FIW and the return strike are also reflected in the potential traces as the two dips in figures 8(*b*) and (*c*) around the same times. The potential curves on the axis and the inner surface of the tube are nearly identical because the high electron density spreads the electric potential across the radius of the capillary tube. On the other hand, the electric fields at these two locations have different characteristics. On the axis, only E_z exists and its maximum value is about 7000 Td. The narrow width (in time) of E_z results from both the thinness of the FIW front as well as its high speed. On the inner surface of the capillary, E_z is smaller with a maximum around 2500 Td with a similar shape as that on the axis. The radial electric field E_r is, however, much higher, about 10 000 Td, and has much wider extent, which corresponds to the larger axial extension of the high E_r region as shown in the figure 6.

4. Concluding remarks

The development of a FIW driven by nanosecond voltage pulses in a capillary tube filled by synthetic air at moderate pressure (27 mbar) was investigated by experimental measurements and 2D numerical modelling. The computed velocity of the FIW front, about 1.4 cm ns^{-1}, and the shape and value of the transmitted electrical current, about 80–90 A at the peak, agree well with values measured in the experiments. The numerical modelling describes the detailed FIW front
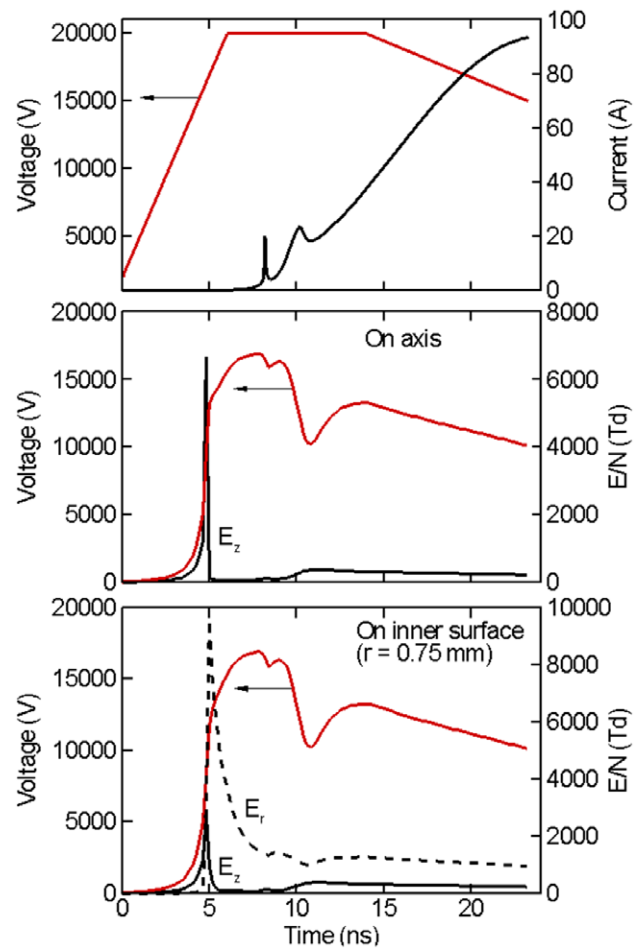

Figure 8. Characteristics of the FIW. (*a*) The HV electrode voltage and transmitted current of the FIW capillary discharge. The time dependences of potential and electric fields (radial, E_r, and axial, E_z) on (*b*) the tube axis and (*c*) the inner surface at $z = 32$ mm from the HV electrode tip.

structure, the current signatures of the forward and backward strikes, as well as the smoothing of the potential observed in the local electric potential measurement produced by the capacitive probe. In addition, the results from this

J. Phys. D: Appl. Phys. **47** (2014) 365202

A V Klochko *et al*

simulation provide some insight in the early phase, spatially inhomogeneous plasma parameters.

Acknowledgments

References

[1] Starikovskaia S M and Starikovskii A Yu 2010 Plasma-assisted ignition and combustion *Handbook of Combustion* vol 5 *New Technologies* ed M Lackner *et al* (Weinheim: Wiley) p 71

[2] Adamovich I V, Choi I, Jiang N, Kim J-H, Keshav S, Lempert W R, Mintusov E I, Nishihara M, Samimy M and Uddi M 2009 Plasma assisted ignition and high-speed flow control: non-thermal and thermal effects *Plasma Sources Sci. Technol.* **18** 034018

[3] Kosarev I N, Aleksandrov N L, Kindysheva S V, Starikovskaia S M and Starikovskii A Yu 2008 Kinetics of ignition of saturated hydrocarbons by non-equilibrium plasma: CH_4-containing mixtures *Combust. Flame* **154** 569

[4] Popov N A 2011 Fast gas heating in a nitrogen–oxygen discharge plasma. Part I. Kinetic mechanism *J. Phys. D: Appl. Phys.* **44** 285201

[5] Burnette D, Montello A, Adamovich I V and Lempert W R 2014 Nitric oxide kinetics in the afterglow of a diffuse plasma filament *Plasma Sources Sci. Technol.* **23** 045007

[6] Anikin N B, Starikovskaia S M and Starikovskii A Yu 2006 Oxidation of saturated hydrocarbons under the effect of nanosecond pulsed space discharge *J. Phys. D: Appl. Phys.* **39** 3244–52

[7] Mintoussov E I, Pendleton S J, Gerbault F G, Popov N A and Starikovskaia S M 2011 Fast gas heating in nitrogen–oxygen discharge plasma. Part II. Energy exchange in the afterglow of a volume nanosecond discharge at moderate pressures *J. Phys. D: Appl. Phys.* **44** 285202

[8] Rusterholtz D L, Lacoste D A, Stancu G D, Pai D Z and Laux C O 2013 Ultrafast heating and oxygen dissociation in atmospheric pressure air by nanosecond repetitively pulsed discharges *J. Phys. D: Appl. Phys.* **46** 464010

[9] Pai D Z, Lacoste D A and Laux C O 2010 Transitions between corona, glow, and spark regimes of nanosecond repetitively pulsed discharges in air at atmospheric pressure *J. Appl. Phys.* **107** 093303

[10] Vasilyak L M, Kostyuchenko S V, Kudryavtsev N N and Filyugin I V 1994 Fast ionisation waves under electrical breakdown conditions *Phys. Usp.* **37** 247–68

[11] Starikovskaia S M, Anikin N B, Pancheshnyi S V, Zatsepin D V and Starikovskii A Yu 2001 Pulsed breakdown at high overvoltage: development, propagation and energy branching *Plasma Sources Sci. Technol.* **10** 344–55

[12] Lagarkov A N and Rutkevich I M 1994 *Ionization Waves in Electric Break-down of Gases* (New York: Springer) chapter 4

[13] Takashima K, Adamovich I V, Xiong Z, Kushner M J, Starikovskaia S M, Czarnetzki U and Luggenhoelscher Dirk 2011 Experimental and modeling analysis of fast ionization wave propagation in a rectangular geometry *Phys. Plasmas* **18** 083505

[14] Klochko A V, Salmon A, Lemainque J, Popov N A, Booth J-P, Xiong Z, Kushner M J and Starikovskaia S M 2014 Experimental and numerical study of fast gas heating and O atom production in a capillary nanosecond discharge *Proc. 52nd AIAA Aerospace Science Meeting (National Harbor, MD)*

[15] Anikin N B, Pancheshnyi S V, Starikovskaia S M and Starikovskii A Yu 1998 Breakdown development at high overvoltage: electric field, electronic level excitation and electron density *J. Phys. D: Appl. Phys.* **31** 826–33

[16] Xiong Z, Robert E, Sarron V, Pouvesle J-M and Kushner M J 2012 Dynamics of ionization wave splitting and merging of atmospheric-pressure plasmas in branched dielectric tubes and channels *J. Phys. D: Appl. Phys.* **45** 275201

[17] Xiong Z and Kushner M J 2012 Atmospheric pressure ionization waves propagating through a flexible high aspect ratio capillary channel and impinging upon a target *Plasma Sources Sci. Technol.* **21** 034001